Journal of Applied Fluid Mechanics, Vol. 11, No. 4, pp. 929-942, 2018.
Available online at www.jafmonline.net, ISSN 1735-3572, EISSN 1735-3645.
DOI: 10.29252/jafm.11.04.28509

Multi-Objective Optimization of Two-Stage Centrifugal Pump using NSGA-II Algorithm

M. Benturki†, R. Dizene and A. Ghenaiet

Laboratory of Energetic Mechanics and Conversion Systems, Faculty of Mechanical Engineering and Process Engineering, University of Science and Technology Houari Boumediene, BP 32 El Alia, 16111 Bab Ezzouar, Algiers, Algeria

†Corresponding Author Email: bentumoh@yahoo.fr

(Received October 11, 2017; accepted January 22, 2018)

ABSTRACT

Improving the efficiency and suction capability of a multistage centrifugal pump poses a major challenge for the designer of this type of equipment. This paper deals with the optimization of a two stage centrifugal pump using Non-dominated Sorting Genetic Algorithm II (NSGA-II), coupled with three-dimensional Reynolds-averaged Navier-Stokes (3D-RANS) flow solver. The first stage comprises a suction impeller with a diffuser while the second stage is formed by a second impeller connected to a volute. Both impellers are of different dimensions and are inter-connected by a return channel. This arrangement increases the number of varying parameters and thus can add further constraints on the overall optimization process; as a result, a high computational complexity of NSGA-II and a higher computational fluid dynamics (CFD) simulation cost is incurred. In order to save running time, optimization with CFD simulations are performed on each stage separately shall enable to obtain better parameterization flexibility; therefore, permitting to adopt only three objective functions in as well as limiting other geometrical constraints. The objectives of this study are to maximize the head and hydraulic efficiency at a time where the net positive suction head inception ($NPSH_i$) is kept to minimum. The overall efficiency as well as the head of the optimized pump were increased by 9.8% and 15.7%, respectively, at best efficiency point (BEP) (rotational speed N=2600 rpm); the $NPSH_i$ of suction impeller was reduced by 13.6%. At N=1450 rpm (BEP), an improvement of 14.9% in the head and 6.52% for the overall efficiency is observed. An important improvement in performance at different operating flow rates was obtained; this was in addition to other enhancements in the volumetric and hydraulic efficiencies. Unsteady CFD simulations were also performed to predict fluctuations in the pressure field, leakage flows and interactions between impellers and collectors. The obtained results were in agreement with experimental data. The head fluctuation of the optimized pump was also reduced by 22.5% in amplitude; this was favored by the presence of a tapered blade towards the trailing edge and the extended radial gap by 4.86% between the second impeller and cutwater, which was caused by the reduction of the impeller diameter.

Keywords: Multi-objective optimization; Two-stage centrifugal pump; Unsteady; CFD; NSGA-II; $NPSH_i$.

NOMENCLATURE

BEP	best efficiency point
C	absolute velocity
C_p	pressure recovery coefficient
Cu	peripheral component of C
d	diameter
DF	disk friction
e	thickness
f(x)	objective function
Gen	generation
H	head rise in the stage or multistage pump
h	hydraulic
LE	leading edge
$NPSH_i$	net positive suction head inception
Pop	population size
Q	volumetric flow rate
Q_{SP}	leakage flow rate through seal
t	time
TE	trailing edge
U	circumferential velocity
v	volumetric
β_b	blade angle
η	efficiency
ω	angular rotor velocity
Θ	wrap angle
p	pressure
M	meridional distance

1. INTRODUCTION

Pumps and turbo-pumps are used in many technological areas and cover a wide range of applications such as thermal power generation, nuclear, propulsion, marine and water supply. Understanding the internal flows in pumps permits an improvement in the performance and thus reducing the overall operating cost. CFD is classified as one of the most important tools used to design efficient turbomachines. CFD is able to predict highly complex flows such as secondary flows, flow separations and leakages, which are considered as the primary sources of losses in pump; the technique is also used to study the interactions between the impellers and collectors. CFD facilitates the findings of essential performances of pump prior to manufacturing the prototype and adjusting the geometry afterwards.

The process of optimization consists of selecting the best solutions from a pool of candidate solutions. Several algorithms have been developed to accelerate the optimization process, to efficiently search the design space, and to decrease the number of evaluation points. One approach often used to rapidly explore the design space and obtain the best solutions is to use Multi-Objective (MO) evolutionary algorithms. Such approach was proven useful for solving a number of engineering problems. Most evolutionary algorithms are robust; hence, they tend to provide distinct problem solving advantages during the development stage. Among the most prominent algorithms are the Pareto Archived Evolutionary Strategy (PAES) (Knowles *et al.* (1999)), Strength Pareto Evolutionary Algorithm (SPEA-2) (Zitzler *et al*. (1998)) and Srinivas *et al*. (1995) proposed NSGA algorithm, which proved to be a landmark in the history of MOEA algorithms; the latter version was followed by the development of a faster one, NSGA-II (Deb *et al*. (2002)). All those algorithms were developed using the concept of Pareto dominance that efficiently combines the elitists preserving approach and the crowding distance (CD) operator in order to maintain diversity and uniformity. NSGA-II was developed to reduce time, complexity and to improve convergence towards the best Pareto front (Fang *et al*. (2008)). An efficient integrated optimization platform based on CFD simulation was first proposed by Hirsch *et al.* (2006), the latter used NSGA-II and Artificial Neural Network (ANN) to create an approximation model for a multipoint optimization process applied to the impeller of a centrifugal pump; the model was used to maximize the hydraulic efficiency as well as the head, and to also minimize $NPSH_i$ via considering two operating points and 36 input parameters. The optimal impeller resulted in 8.5% increase in head and 0.9% gain in hydraulic efficiency with 23% reduction in $NPSH_i$.

Huang *et al*. (2015) used a modified NSGA-II algorithm coupled with a dynamic crowding distance (DCD) and 3D inverse design method to optimize a mixed flow pump impeller with the aim to maximize the hydraulic efficiency and head. The authors adopted a radial basis neural network (RBNN) to approximate the objective function with 82 training samples. Zhang *et al*. (2011) developed a multi-objective method, combining ANN with NSGA-II to improve the performance of helico-axial multiphase pump. The obtained results were compared to the original design, which resulted in a 10% and 3% increase in head and overall efficiency, respectively. Nourbakhsh *et al*. (2011) used a particle swarm optimization (PSO) method and NSGA-II algorithm with a neural network meta-model to find the Pareto front of two conflicting objectives of centrifugal pumps: efficiency and Net Positive Section Head Required ($NPSH_r$). The Pareto frontiers indicated that lower $NPSH_r$ lead to lower efficiency.

The aforementioned studies provided solutions for the partial optimization of a single component of centrifugal pumps. The present work focuses on optimizing a two-stage of a multistage pump; thus, allowing to predict the interactions between the different components. Each stage is highly parameterized, taking into account all variables influencing the hydraulic and mechanical behavior of the pump. Modeling the volute, diffuser and its flow exits located in sidewall present a major challenge during the optimization process. The purpose of this study is to find, through the utilization of CFD and NSGA-II, an optimum design derived from two Pareto fronts. CFD validation was achieved through comparison of experimental data and the unsteady CFD simulation of the original pump; this was followed by a complete CFD analysis of the optimal multistage pump which showed an improved performance following an internal flow field comparison.

2. DESCRIPTION OF THE PUMP MODEL

SK80 pump model (Figs. 1(a) and 1(b)) is a horizontal multistage centrifugal pump designed and tested by Rovatti Pompe; the pump has a diffuser type casing and an enclosed impellers. The second stage impeller has a larger diameter (d_2=265 mm) compared to that of the first impeller (d_2=205 mm). The fluid coming from the second impeller is radially discharged by the diffusing channel of the volute. Each stage casing has a radial impeller, a diffuser and a return channel that forms a unit which is capable of orienting the fluid to the next stage. The liquid flows laterally from the diffuser, so that it enters the return channel (equipped with 6 blades) at 90° deflection, as shown in Fig. 1(c). The front shroud leakage Q_{SP1} and Q_{SP4} flow from the exits of impellers and return to the inlet through the annular gap seals residing between the wear rings and the rotating sidewalls (Figs. 1(d) and 1(e)). The rear hub leakage Q_{SP2} and Q_{SP5} flow through the annular seals towards the balancing chamber. Seven holes are drilled to direct the leakages to the impeller suction zone. The inter-stage leakage Q_{SP3} flows from the return channel to the balance chamber, and then to the inlet of the impeller (Fig. 1(d)). At the nominal operating point: H=96.5 m, N=2600 rpm and Q=84m^3/h, while (H=34.5 m) and

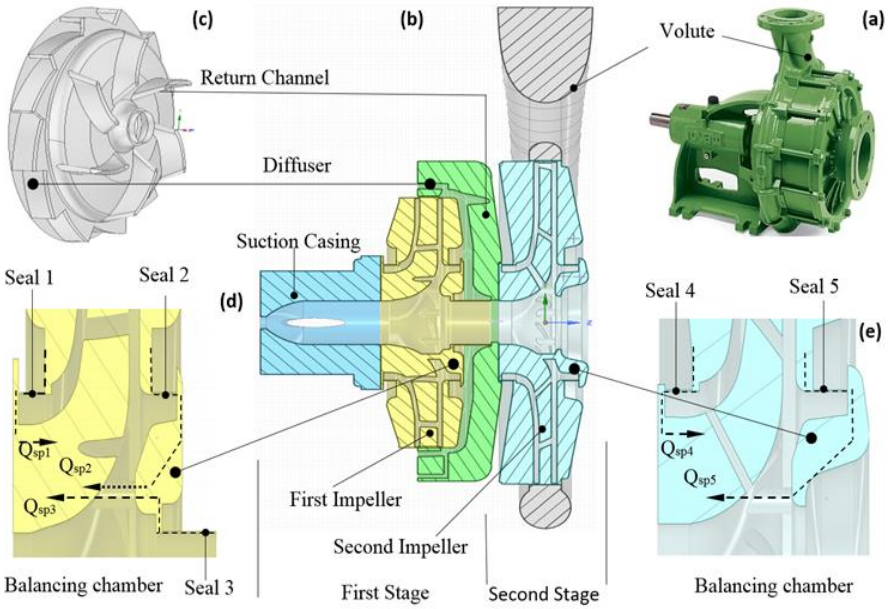

Fig. 1. (a) 3d view of SK80 multistage centrifugal pump, (b) cross sectional view, (c) diffuser and return channel, (d) leakage flows of the first stage and (e) leakage flows of the second stage.

(H=62 m) are the head of the first stage and second stage, respectively. The specific speeds of the first and second stage are; 28 and 18, calculated by the formula: Nq=N.Q0.5/H0.75; H (m), Q(m3/s) and N(rpm).

3. THREE-DIMENSIONAL CFD ANALYSIS

The multistage simulations were all performed using ANSYS CFX 14.5. Initially, CAD models were obtained by ANSYS Design Modeler 14.5. The flow channels with casing, seals and balance chambers were modeled separately then assembled; solid geometries such as those of the blades and sidewalls were extracted from the fluid model. The pump was split into eleven components including two impellers and five seals, representing the rotating domains. The suction casing, diffuser, return channel and volute were kept stationary. To save computing time, the seals, diffuser and return channel were set periodic whereby each fluid passage was composed of two blades; symmetry was used to design the half suction casing. The CAD models are presented in Fig. 2(a), showing fifteen interfaces between the rotors and stators.

To reduce running time, the periodic models were adopted to stages using a one passage for both the impeller blade and diffuser. The boundary conditions are depicted in Figs. 2(b) and 2(c); the coupling between the rotating and stationary domains was ensured by one interface. For an original and optimum centrifugal multistage pump, medium, unstructured tetrahedral and pyramidal meshes (Figs. 3(a), 3(b) and 3(c)), associated with three prism layers near the walls, were generated using the log-law wall function; this was performed in order to capture the boundary layer separation. The y+ wall distance estimation was assigned a value ≤ 20 for the whole computational domains. The seals were meshed with hexahedral elements (Fig. 3(d)). The orthogonal quality was set between 0.2 and 1; more than eighty percent of cells had an orthogonal quality greater than 0.6. ANSYS Meshing 14.5 generated 13.41 million cells which were used for the original multistage pump; this was compared to 14.52 million cells for the optimal pump. The mesh increase was owing to the first impeller respecting minimum orthogonal quality; the detailed grid is given in Table 1. The previous multistage strategy of meshing was adopted to mesh the stages during the optimization process; the number of cells changed for each point of design but stayed close to the initial topology, counting 1.32 and 0.86 millions of cells for the first and second stage, respectively. ANSYS CFX 14.5 was used to solve the incompressible steady and unsteady 3D-RANS equations using Menter's shear stress transport (SST) turbulence model. This approach was previously validated by many researchers from around the world, for example, a multistage pump investigated by Feng *et al*. (2009), gave results which were in agreement with particle image velocimetry (PIV) and laser dopler velocimetry (LDV) measurements, at different operating points. The time step required for the unsteady simulation corresponded to three degrees of impeller rotation and between 3 and 6 impeller revolutions until achieving convergence stability. For all models, the boundary conditions were set as follows: (i) the total pressure at the inlet, (ii) the mass flow rate at the outlet, and (iii) the frozen-rotor method was applied at the rotor-stator interface for all steady state simulations. However, the transient rotor-stator condition was also specified at the interface during unsteady simulations. All solid walls were non-slip, while the external walls of the impellers and shroud seals had counter rotating walls. An Upwind scheme was set for the advection term. The essential conditions necessary for CFD simulations are summarized in Table 2, and also shown in Fig 2.

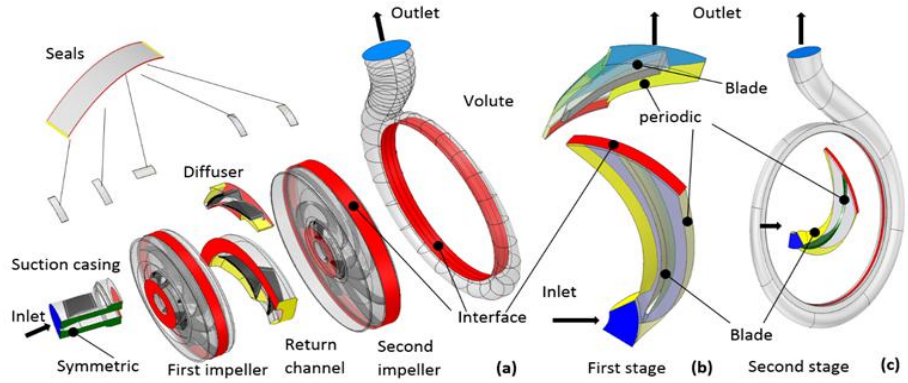

Fig. 2. Cad models with boundary conditions: (a) full multistage pump, (b) first stage domain and (c) second stage domain.

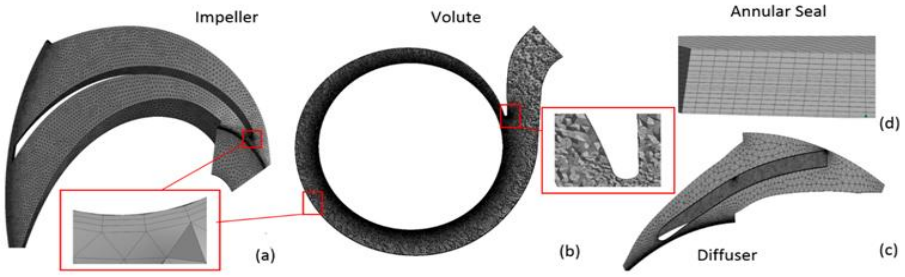

Fig. 3. Tetrahedral, pyramidal and prismatic meshes: (a), (b) and (c); d) hexahedral mesh.

Table 1 Grids details of the original and optimal centrifugal pump

Parts		Suction casing	First impeller	Second impeller	Five seals	Diffuser	Return channel	Volute
Mesh		Tetra - pyramid - Prismatic			Hexa	Tetra - pyramid - Prismatic		
size millions	Original	0.345	3.64	3.11	0.869	4.50	0.585	0.365
	Optimal	0.426	5.56	2.10	0.592	5.35	0.372	0.120

4. PERFORMANCE ANALYSIS

In order to validate numerical model and to evaluate the performances and the objective functions of NSGA-II, all performance parameters were determined by integration and were averaged at various control surfaces, over the total time of revolutions in an unsteady state regime.

The head increase was calculated between the inlet and outlet using the following equation:

$$H = \frac{P_2 - P_1}{\rho g} + \frac{C_2^2 - C_1^2}{2g} \quad (1)$$

Table 2 Operating conditions in the CFD simulations

Parameter	Multistage centrifugal pump	Stage of pump
Flow regime	Steady and unsteady	Steady
Turbulence model	SST	SST
Total pressure inlet, atm	1	1
Outlet flow rate (N=2600 rpm), m^3/h	36 - 42 - 48 - 54 - 60 - 66 - 72 - 84 - 96	84
Outlet flow rate (N=1450 rpm), m^3/h	24 - 30 - 36 - 42 - 48 - 54 - 60 - 66 - 72	-
Flow medium (20° C) ; Water	ρ=997 kg/m^3	ρ=997 kg/m^3
Interface	GGI-frozen rotor	GGI-frozen rotor
	Transient rotor stator	
Rotation speed (N), rpm	1450 and 2600	2600
Convergence criteria (RMS)	10^{-4}	10^{-4}
Number of Revolution	3 to 6	-
Time step, s	$3.448.E^{-4}$ (1450 rpm) - $1.923.E^{-4}$ (2600 rpm)	-

Where P_1 and P_2 are the averaged static pressures, ρ is the water density and g is the gravitational acceleration. C_1 and C_2 are the average absolute velocity at the inlet and outlet, respectively.

During the optimization process, only the static term at the exit of the stage was considered; the total-static performance permitted the utilization of the minimum objective functions without the requirement to assign another objective function for the outlet velocity of the collector or its static pressure recovery coefficient.

The volumetric efficiency at each stage can be evaluated by:

$$\eta_v = \frac{Q}{Q + Q_{SP}} \tag{2}$$

Whereby Q is the volumetric flow rate and Q_{SP} is the leakage flow rate through the annular seal.

The hydraulic efficiency of a stage pump is calculated using the following equation:

$$\eta_h = \frac{gH}{U_2 Cu_2 - U_1 Cu_1} \tag{3}$$

Whereby U is defined as the circumferential speed and Cu is the averaged circumferential component of absolute velocity; 1, 2 are the leading edge and trailing edge surfaces of the impeller, respectively.

The impeller power is known by the following equation:

$$P_I = \omega M_I \tag{4}$$

Where M_I is the torque of the whole impeller surface and □ is the rotational speed [rad/s].

The equation for the disk friction power is described as follows:

$$P_{DF} = \omega M_{DF} \tag{5}$$

Where M_{DF} is the equivalent disk friction torque of the impeller.

The required shaft power is described using the following equation:

$$P_{shaft} = P_I + P_{DF} \tag{6}$$

The overall efficiency is defined as follows:

$$\eta = \frac{\rho g Q H}{P_{shaft}} \tag{7}$$

The static pressure recovery coefficient C_P is used to evaluate the performance of the diffuser and volute using the following formula:

$$C_P = \frac{P - P_2}{0.5 \rho C_2^2} \tag{8}$$

Where P_2 is the average static pressure and C_2 is the average absolute velocity at the impeller exit.

The cavitation inception is observed at $P_{min}=P_v$, the point where the first vapor bubbles are generated. $NPSH_i$ is the minimum value to operate without cavitation, and is defined by:

$$NPSH_i = \frac{P_{t1} - p_{\min}}{\rho g} \tag{9}$$

Where P_{t1} is the inlet total pressure and P_{min} is the minimum pressure in the impeller.

4.1 CFD Validation

Figure 4 depicts the relative error of the head and overall efficiency at different rotational speeds and flow rates. The predicted curves (H and η) followed the same trend as those of the experimental results. According to (Fig. 4(a)), a good agreement between predicted values and the experimental ones was observed at N= 2600 rpm; a better accuracy was obtained at the nominal design point. The deviations in overall efficiency was - 0.01% at BEP; however, the value was kept within range (between - 0.8% and +0.98%) off-BEP. The deviation for the head curves was -0.07% at BEP and less than 0.936% for all operating flow rates. At low speed (N=1450 rpm, Fig. 4(b)), the deviation was +0.55% and -2.6% for

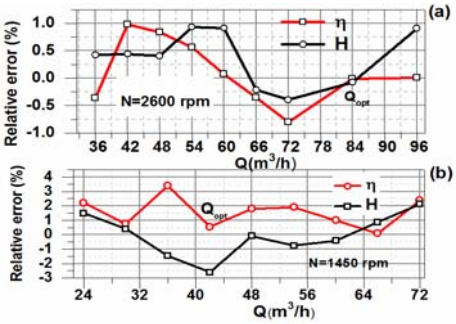

Fig. 4. Relative error versus the flow rate and rotational speed.

overall efficiency and head. Off-BEP, the numerical predictions deviated from the experimental values by a maximum of 3.4% for efficiency, while head deviation varied between -2.60% and 2.13%. CFD predictions used the same mesh for both rotational speeds; thus, resulting in differences within the relative error range. When the rotational speed was less than the nominal speed; this can lead to flow deceleration as well as separation of boundary layers. Therefore, a much more refined mesh may be required for each flow rate. The previous analysis consolidated the idea to perform the optimization process at the optimum operating BEP, i.e., Q=84 m^3/h and N=2600 rpm. This accuracy was perhaps owing to the quality of selected turbulence model, which prompted a successful prediction in the flow separation; this was further confirmed by other studies by Feng *et al*. (2009). In addition to the interaction between the leakage flow and the main flow, which could modify the inlet velocity field and through the impeller passage, the interaction between the impellers and collectors can also play part in affecting the blade loading.

5. OPTIMIZATION PROCEDURE

The procedure developed to optimize SK80 centrifugal pump is presented in Fig. 5. The optimization procedure steps are as follows:

1. Modeling the original pump without neglecting any details (Fig. 2(a)), followed by analyzing the steady state and unsteady internal flows. Finally, predict the overall performances and compare them to the available experimental ones.

2. Extracting the two stages from the initial pump and creating the two independently parameterized models. The first stage is formed by the first impeller and the diffuser (Fig. 2(b)) while the second stage is formed by the second impeller connected to the volute (Fig. 2(c)). This method enables : (i) to reduce

the NSGA-II complexity of computation by adopting three objective functions and minimizing the constraints, (ii) to obtain better parameterization flexibility, and (iii) to save running time of the CFD simulations. CFD analysis was performed for each stage separately with the aim of computing only three objective functions used by its own NSGA-II algorithm, and to obtain a quick convergence towards the best Pareto front.

3. Optimizing each stage using NSGA-II algorithm coupled with ANSYS Workbench. The optimum design is selected from the Pareto fronts, according to the criteria which required reduction in the impellers diameters, their axial distance and the height of the volute relative to the shaft.

4. Two sets of criteria are to be satisfied after full CFD analysis for the new optimal pump. Firstly, the continuous operation should be in the range $0.12 < Q/Q_{opt} < 1.14$ at N=2600 rpm, as specified by the pump characteristics test. Secondly, ensuring that the head stability is within the required operating range; the stability condition is defined as:

$$\frac{\partial H}{\partial Q} \leq 0 \tag{10}$$

5.1 Multi-Objective Optimization using NSGA-II algorithm

The optimization work was performed by coupling NSGA-II with ANSYS workbench 14.5; was able to create geometry and to mesh and to solve the 3D RANS equations for each pump stage (Figs. 2(b) and 2(c)). The stage performance was evaluated in a steady state regime at BEP (Q_{opt}=84 m^3/h, N=2600 rpm). The general formula for a multi-objective optimization problem is mathematically defined using the following equation:

Maximize / Minimize $f_j(x)$, j = 1, *m*

Subject to $g_k(x) \geq 0$, k =1, *l*

$$x_i^{min} \leq x_i \leq x_i^{max} \text{ , i = 1, } n \tag{11}$$

Where $f_j(x)$ are the objective functions, *m* is the number of objectives, x is a vector whose *n* components are the design or decision variables, and $g_k(x)$ are the constraints. (*l*) is the number of constraints.

The objectives required for the optimization process are: (i) maximizing the head (H), (ii) maximizing the hydraulic efficiency (η_h), and (iii) minimizing $NPSH_i$. This can be written in the following way:

$f_1(x)$ = Max H

$f_2(x)$ = Max η_h

$f_3(x)$ = Min $NPSH_i$ (12)

The suggested method provided an open choice from both Pareto frontiers. Additional constraints have been considered to further improve the mechanical strength of the optimum design. The fatigue of blades and pump structure was primarily caused by pressure pulsations; to reduce the alternating stress, the spaces between impellers and collectors must be enlarged by reducing the impellers' diameter ($d_2 \leq$ 205 mm and $d_2 \leq$ 265 mm). Under loading conditions, the rotor was caused to deflect; thus, creating high alternating bending stresses. In order to keep the impellers away from rubbing against the wear ring seals, the shaft length must be reduced ($Z_0 \leq$ 32 mm and $Z_0 \leq$ 30 mm). The volute discharge nozzle could also deflect under the influence of

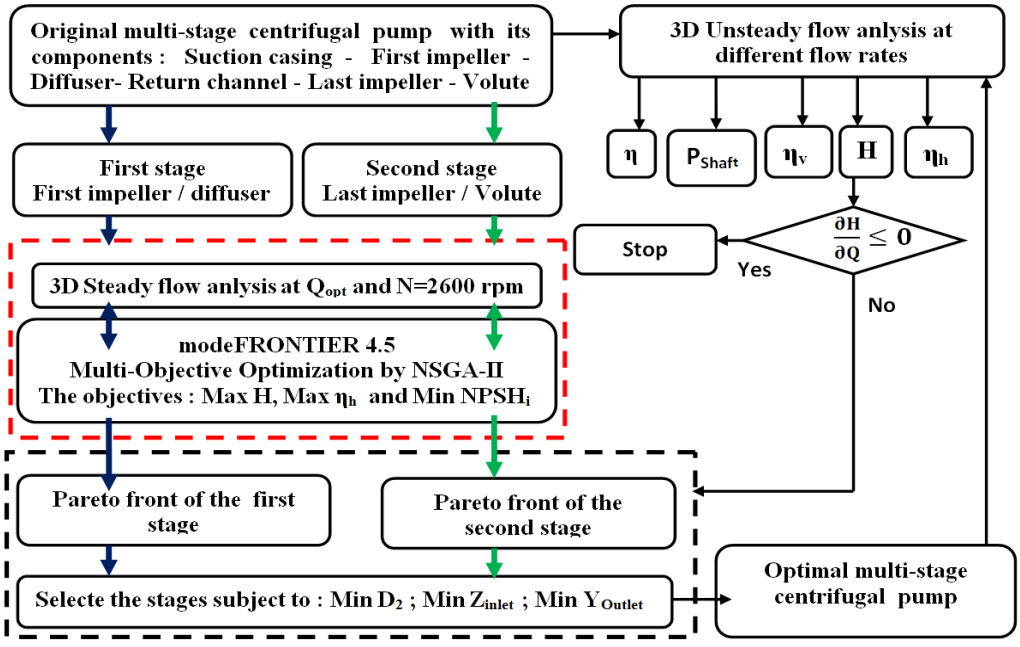

Fig. 5. Schematic presentation of the optimization process.

pipeline forces; therefore, by minimizing the height of the volute, aimed to reduce the bending stress in the diffusing channel of SK80 pump ($Y_{outlet} \leq$ 265 mm).

NSGA-II code was integrated with FRONTIER 4.5

software, a full integration platform for multi-objective optimization algorithms. The software provided a seamless coupling with CAD design and other analyses tools; it also enabled the automation of the design simulation process, performed advanced data mining, and facilitated decision making.

The procedure for NSGA-II algorithm was previously outlined by Deb *et al.* (2002). Initially, a first parent population P_0 of size (Pop) was created randomly. The population P_0 was sorted by means of their objective functions in the first Pareto front F_1, to form rank (r_1), which was filled only by non-dominated solutions (best solutions). Then, a second front F_2 was formed, which included only the individuals dominated by the individuals in F_1. The non-dominated sorting was repeated until the last individuals were assigned to their corresponding fronts. The genetic operators were implemented stepwise. First, the selection was performed by a crowded tournament selection, where the solutions were compared according to their rank together with the crowding distance (d_i) that measured the population density around a one solution. Consequently, the best solutions were favored and their diversity was ensured over the Pareto front; afterwards, the crossover probability operator (P_c=0.9) was applied to create offsprings from the above selected population. Only few parents were preserved. Finally, the mutation probability operator emphasized the diversity. Lower P_m values (P_m=1/n, where n is the number of variables), can slightly perturb the offspring solution. At this stage, the first child population Q_0 of size (Pop) was created. P_0 and Q_0 were then combined (P_0 U Q_0) to form population R_0 of size (2Pop); the previous procedure was applied to classify the entire population R_0. A new generation of parent population P_1 of size (Pop) was generated. The same procedure could be repeated with P_t parent until the maximum number of generations was reached. Noting that in the selection step, feasible solutions, without violation of constraints, were favored. A large population size provided a high diversity which gave more opportunities to converge towards the global optimal. A series of numerical experiments were performed in order to evaluate the influence of the population size on the genetic algorithm (GA). Shi *et al*. (2012) proposed that the minimum population size (Pop=3n) gave an estimated value of Pop=147; the optimal population size (Pop) and optimal generation (Gen) were empirically computed using the models of Cvetković (1994). Therefore, the estimated values are Pop=131 and Gen=14 at the mean values of parameters. The optimal population was calculated in the range 145 ≤ Pop ≤ 290 with n=49 parameters (according to Jarmo (1992) model). The performance of NSGA-II was analyzed to determine the optimal population size from two populations, generated quasi-randomly using SOBOL algorithm (Bratley *et al* (1988)); a uniform design space was created while rejecting all unfeasible designs that did not satisfy the geometrical constraints. From Table 3, an initial population Pop=350 revealed superiority in terms of average objective functions, geometry failure, and feasible designs, when compared with Pop=500; this was due to the perfect distribution of variables over their corresponding ranges without overcrowding.

Table 3 NSGA-II Performance of the first stage with two population size

Generation (Gen)	Gen=1		Gen=2	
Population (Pop)	350	500	350	500
Feasible (%)	27	19.6	38	24
Unfeasible (%)	72	55.6	59	58
Failure (%)	1	24.8	9	17.8
Mean ΔH/H (%)	4.37	3.31	7.8	3.8
Mean $\Delta\eta_h/\eta_h$ (%)	23.5	23	25.4	25.3
Mean $NPSH_i$ (m)	12.4	12.6	10.3	11.1

Albeit Pop was created using genetic operators in the second generation, the obtained results confirmed the same tendency, with more feasible designs generated for Pop=350. In the second stage, simulation comparison between two population sizes Pop=600 and Pop=350, proved the same behavior as described above; for Pop=350, the rate of feasible point of design was 4.6% at Gen=1, reaching 18.8% at Gen=4, compared to 0.5% at Gen=1 and 8% at Gen=4 for Pop=600. Clearly, Pop=350 was better suited for this study. According to convergence history, after fifteen generations (Gen=15), the mean and best objective function of the hydraulic efficiency varied slightly; thus, NSGA-II runs were limited to Gen=18.

5.2 Geometry Parameterization

A variety of shapes were generated using few design variables as possible. With the help of ANSYS Design modeler, a simplified CAD model was generated and parameterized. To avoid failures in the geometry generation, some constraints were created between parameters. In total, 42 parameters were used to define the geometry of the first stage with 15 constraints, compared to 49 parameters and 16 constraints for the second stage. In this study, the parameters r, θ and z are the radial, angular and axial locations, respectively; (e) is the blade thickness (Figs. 6(a) and 6(b)). dM is the meridional distance, as depicted in Fig. 6(a). dM' is the normalized meridional distance, defined by the following equations:

$$dM = \sqrt{dr^2 + dz^2} \quad \text{and} \quad dM' = \frac{dM}{r} \tag{13}$$

The warp angle (θ) is correlated against the blade angle (β_b); thus, controlling the blade curvature (Fig. 6(b)), defined by the following formula:

$$d\theta = \frac{dM'}{\tan(\beta_b)} \tag{14}$$

5.2.1 Impellers Parameterization

The meridional parametric model consists of a hub and shroud curves (Fig. 6(a)). Each B-Spline curve was created by six control points CP_0, CP_1, CP_2, CP_3, CP_4 and CP_5. Only CP_0, CP_2 and CP_5 were free

to move; the other points could move along two straight lines, so, each curve had a vector design x= (Z_0, Z_1, Z_2, Z_5, R_0, R_2, R_3, R_4, R_{TE}). The position Z_{le} and the inclination angle (φ) were used to control the leading edge curve. The trailing edge radius (R_{TE}) was specified as a parameter. The blade was designed from a camber line and the symmetric thickness distribution. Each camber line was fitted with a Bezier curve known from six parameters (Fig. 6(d)): The wrap angles θ_1, θ_3, θ_4 and θ_6 controlled the mean-line curvature by freezing (M').

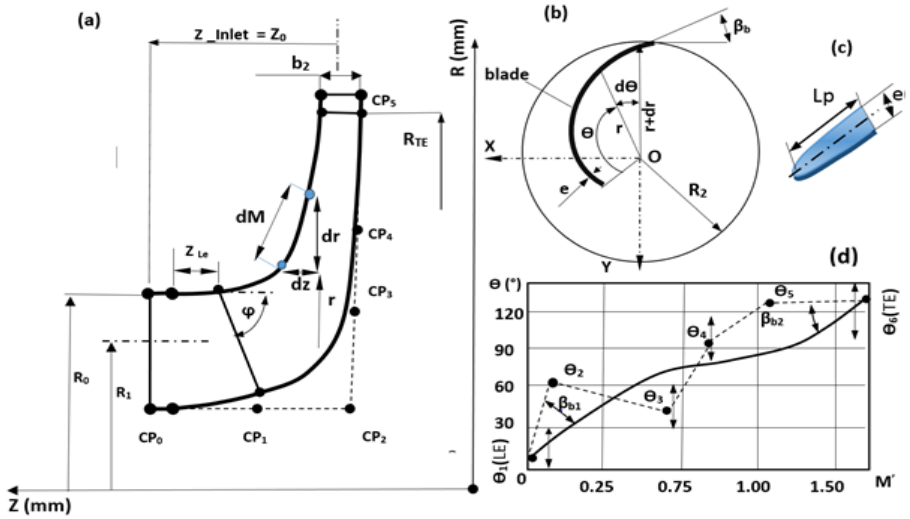

Fig. 6. Impellers parameterization: (a) meridional section, (b) blade angles, (c) LE profile and (d) blade angle parameters.

Also, parameters β_{b1} and β_{b2} represented the leading and trailing edge blade angles. The impeller blade thickness is parameterized by three control points of a Bezier curve; e_1, e_2 and e_m (Fig. 7(c)).

5.2.2 Diffuser Parameterization

The diffuser geometry was parameterized by distances DZ and DR, as depicted in Fig. 7(a). Besides the trailing edge (DTE) location, the parameter ($SR=L_p/e$) controlled the elliptic leading edge shape of the impeller and the diffuser, as shown in Fig. 6(c). The blade distribution angle (β_b), as shown in Fig. 7(b), was defined by the cubic Bezier curves with four control points (β_{b1}, β_{b2}, β_{b3}, β_{b4}). The blade thickness curve of the diffuser is depicted in Fig. 7(c), and parameterized by (e_1, e_1).

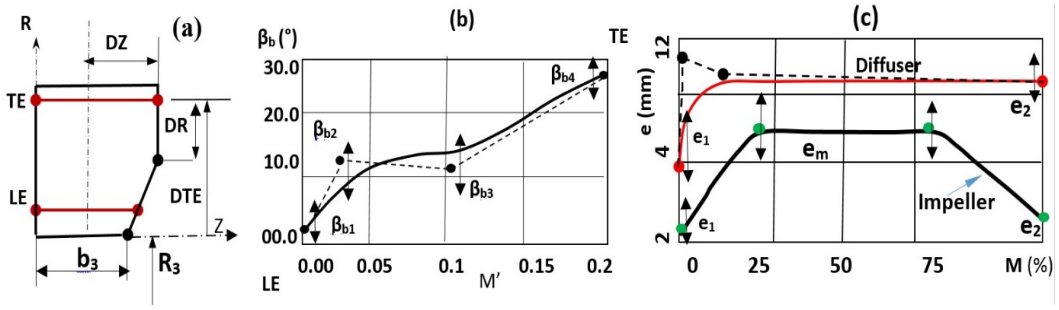

Fig. 7. Diffuser parameters: (a) meridional section, (b) blade angle distribution and c) blade thickness distribution.

5.2.3 Volute Parameterization

The volute geometry comprised of two parts, the spiral and the diffusing channel (Fig. 8(a)); both parts were designed by lofted cross sections. The spiral was defined by eight angular positions (θ). Among the four cross sections forming the diffusing channel, three of them had two degrees of freedom and were parameterized by the distance (X) and the plane angle (ϕ). The outlet was controlled by Y_{outlet} parameter, while all cross sections were parameterized with radii R_θ and R_ϕ, as shown in Figs. 8(b) and 8(c).

The axial gaps between the impellers and collectors were kept constant. The inlets of the collectors were controlled by the outlet of impellers parameters. Some of design variables and their corresponding ranges are shown in Table 4; some constraints between variables are also summarized in Table 5. The parameter ranges were tested using different values in order to respect the standard radial shape of this pump.

The blade curvature angle θ_6 at the impeller exit was assigned the range [95°-121°]. The lower bound enabled to reach the minimum blade length required to maintain a head curve stability; a longer

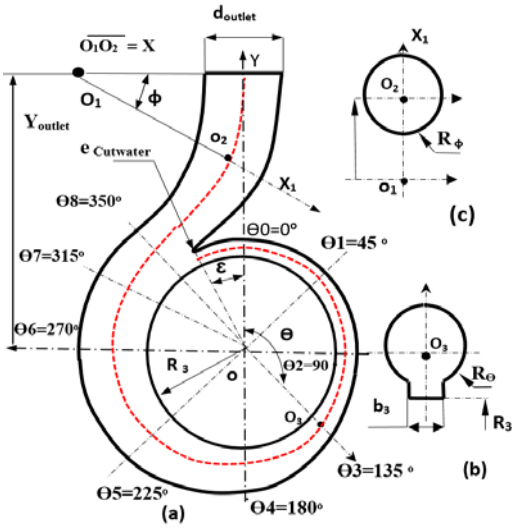

Fig. 8. Volute parameters: (a) volute casing, (b) spiral cross section and (c) cross section of the diffusing channel.

blade at the upper bound can induce a smooth flow without separation, with more pressure being lost through friction. The latter may be compensated by assigning a large TE blade angle; hence, β_{b2} was kept in the range [25°-45°]. Extending the length of the elliptic shape of the blade leading edge can create a favorable pressure distribution, while also enhancing cavitation, as previously discussed by Gülich (2010). Hence, SR was assigned the range [2-8]. The smooth curvature of the meridional shape resulted in a better jet-wake flow at the impeller exit with much less separations. As a result, the B-spline curves were regulated by R and Z distances (Table 5). The diffuser β angle criteria ($\beta_{b\,i+1}-\beta_{b\,i} > 0$; i=1, 3) involved a smooth progression in order to avoid severe curvatures. By applying the thickness criterion ($e_2-e_m>0$), the blade was tapered towards the trailing edge which may lead to reduction in the wake width as well as the pressure pulsation. The flow rate is proportional to the angle (θ). The volute cross-sectional area was kept wide; as a result, the criterion ($R_{\theta\,i+1} - R_{\theta\,i} > 0$; i=1, 7) was satisfied. The condition ($\theta_4 - \theta_3 > 0$) ensured

Table 4 Input variables with their ranges

First impeller (shroud curve, leading edge and trailing edge): [mm] unit; Z, R and e									
Variable	Z_0	Z_2	Z_5	R_0	R_2	R_{TE}	Z_{LE}	φ (°)	SR
Range	28-36	5.5 - 11	4-8	38-45	40 - 48	100 -112	1-7	12-40	2-8
Variable	β_{b1}(°)	β_{b2} (°)	θ_1 (°)	θ_3 (°)	θ_4 (°)	θ_6 (°)	e_1	e_2	e_m
Range	17-37	25-45	13- 27	28 - 48	50 - 80	95 - 121	3 - 5	3 - 8	4-8
Diffuser (First stage): [mm] unit; DZ, DR, DTE and e									
Variable	DR	DZ	DTE	β_{b1} (°)	β_{b2} (°)	β_{b3} (°)	β_{b4} (°)	SR	e_1
Range	8 -21	5 - 12	23-36	4 - 12	10 - 28	10 - 27	15-30	2 - 6	2.5-4.5
Volute (Second stage): [mm] unit; Y, R_θ, R_{outle} and e_{cw}									
Variable	$R_{\theta1}$	$R_{\theta2}$	$R_{\theta6}$	$R_{\theta7}$	$R_{\theta8}$	Y_{outlet}	R_{outlet}	ε (°)	e_{cw}
Range	11-13	11-14	16-21	17-23	19-24	255-270	28 -36	15-26	4-6

Table 5 The Geometry constraints

Stage geometry constraints		
First stage impeller	*Second stage impeller*	*Diffuser*
$R_{i+1} - R_i > 0$; i=2, 4	$R_{i+1} - R_i > 0$; i=1, 3	$\beta_{b\,i+1} - \beta_{b\,i} > 0$; i=1, 3
$R_2 - R_0 > -1.2$ (shroud)	$R_2 - R_0 > -1.2$ (shroud)	$e_2 - e_1 > 0$
$\theta_4 - \theta_3 > 0$	$Z_0 - Z_2 > 0$ (hub)	*Volute*
$e_m - e_1 > 0$ and $e_2 - e_m > 0$	$e_m - e_1 > 0$ and $e_2 - e_m > 0$	$R_{\theta\,i+1} - R_{\theta\,i} > 0$; i=1,7

a backward development for the blade curvature; thus, improving Q-H curve stability and decreasing flow separation.

6. RESULTS AND DISCUSSION

6.1 Pareto Frontiers

The completed Pareto frontiers are depicted in Fig. 10, clearly showing that of the hydraulic efficiency with head (Figs. 10(a) and 10(c)), $NPSH_i$ with hydraulic efficiency (Fig. 10(b)) and $NPSH_i$ with head (Fig. 10(d)). The yellow points marking the design showed unfeasibility owing to geometric restrictions. The two optimal points were selected with regards to previous criteria; a head increase of 28.5% and 24% was assigned to that of the first and the second stage, respectively. Although the gain in hydraulic efficiency was estimated by 12.65% and 0.85%, $NPSH_i$ reduction was set to 13.6% and 18.28%, as depicted in Figs. 10(b) and 10(d). More feasible designs were obtained from the diffuser stage, mainly owing to hydraulic efficiency improvement. These results are explained by the fact that: (i) the diffuser geometry was less curved, (ii) its hydraulic losses depended strongly on incidences at the leading edge, and (iii) the throat area controlling the flow velocity through the passage. The modeling of volute was a complicated task in the optimization process; the flow path was irregular and strongly curved. Often created without respect to the smooth transitions between the lofted sketches, this kind of CAD model can generate more losses owing to the generation of severe

curvatures. The significant improvement of head at most design points are associated with the increase in the impellers' diameters. Sensitivity analyses showed that the best $NPSH_i$ was influenced by the parameters of the suction zones. Firstly, at blade LE, x= (e_1, θ_1 _shroud, $\beta_{b1,}$) and R_0, the parameters were able to reduce flow blockages in the twisted blades. Secondly, the deceleration of flow in the fluid passage, through the throat, and near the high curvature of the shroud curve, strongly depended on the vector design, i.e., x= R_0, e_m, θ_3 (shroud), θ_3 (hub), Z_0, R_2 (shroud). The optimal geometry was different from the initial one (Fig. 9), while all parameters for the two stages were moved (Table 6).

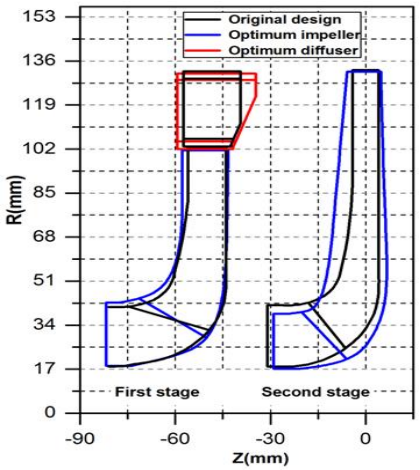

Fig. 9. Optimum and original stages comparison in the meridional plane.

6.2 Original And Optimal Pump Operating Characteristics

Figure 11 depicts the pump head and overall efficiency at different rotational speeds and flow rates. The predicted curves of the original pump

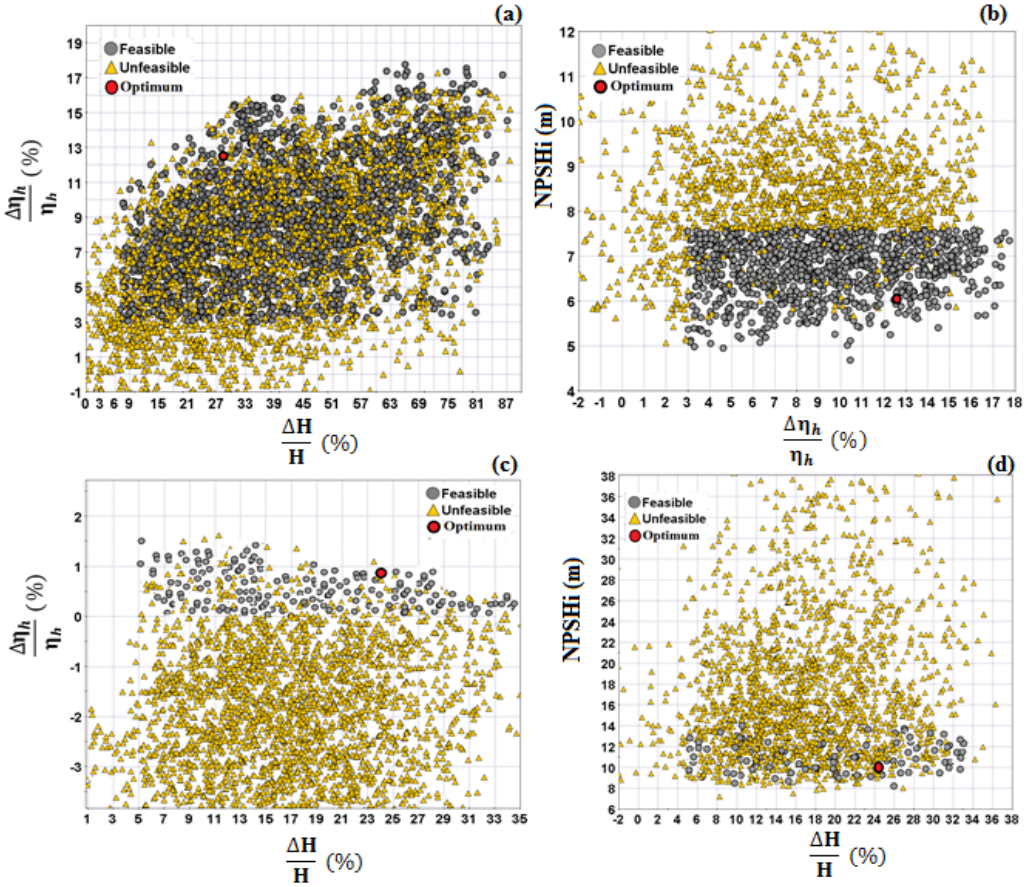

Fig. 10. Pareto fronts of the first stage: (a) head and hydraulic efficiency, (b) hydraulic efficiency and $NPSH_i$; Pareto fronts of the second stage: (c) head and hydraulic efficiency, (d) head and $NPSH_i$.

were in agreement with the experimental results; the performance of the optimal pump significantly increased while the stability of the optimal head curve was satisfying. These results were owing to improvements in the hydraulic and volumetric efficiency, as shown in Fig. 12. Leakages tend to flow radially inwards with high pre-swirl at the side gaps (Fig. 13), this was favored by a reduction in the axial spacing between the impeller sidewalls and the stationary casing which often tends to accelerate the core flow and reduce disk friction losses (Dailey *et al* 1960). The optimum design enabled to extend the operating range above BEP point. With reference to the experimental work presented by Gülich (2010), the author revealed that, reducing the throat are resulted a BEP in

Table 6 Design variables comparison of the impellers and collectors for the original and optimal pump

Parameter	First impeller		Second Impeller	
	Original	*Optimum*	*Original*	*Optimum*
Inlet diameter [d_0], mm	82	85.2	83.5	76.86
Inlet axial distance [Z_0], mm	32	31.7	30	28.97
Mean diameter of leading edge [d_1], mm	37.3	37.9	34.8	31.3
Leading edge thickness [e_1], mm	4	2.5	4	3
Inclination angle of the leading edge [φ], °	21.6	36.9	56.76	51.43
Outlet diameter [d_2], mm	205	201	265	263.88
Outlet width [b_2], mm	12	14.5	8.2	10.7
Mean blade angle of the leading edge [β_{b1}], °	21.5	20.7	39.7	22.5
Mean Blade angle of the trailing edge [β_{b2}], °	33	39.58	27.7	32.18
Blade number [Z_{La}]	7	7	7	7
TE wrap angle [θ],°	107	121	118	121.55

Diffuser parameter	*Original*	*Optimum*	Volute parameter	*Original*	*Optimal*
LE blade angle [β_{b1}], °	10.7	9.18	Cutwater thickness [e_{cw}], mm	5	4.46
Inlet width [b_3], mm	15	17.5	Outlet diameter [d], mm	65	60
LE thickness [e_1], mm	3	3.63	Outlet height [Y], mm	260	259.5
Inlet diameter [d_3], mm	206	204	Inlet width [b_3], mm	22	22
Wrap angle [θ], °	40	47	Inlet diameter [d_3], mm	272	267.8
Blade number [Z_{Le}]	12	12	Angle of cutwater [ε],°	21.44	19.6

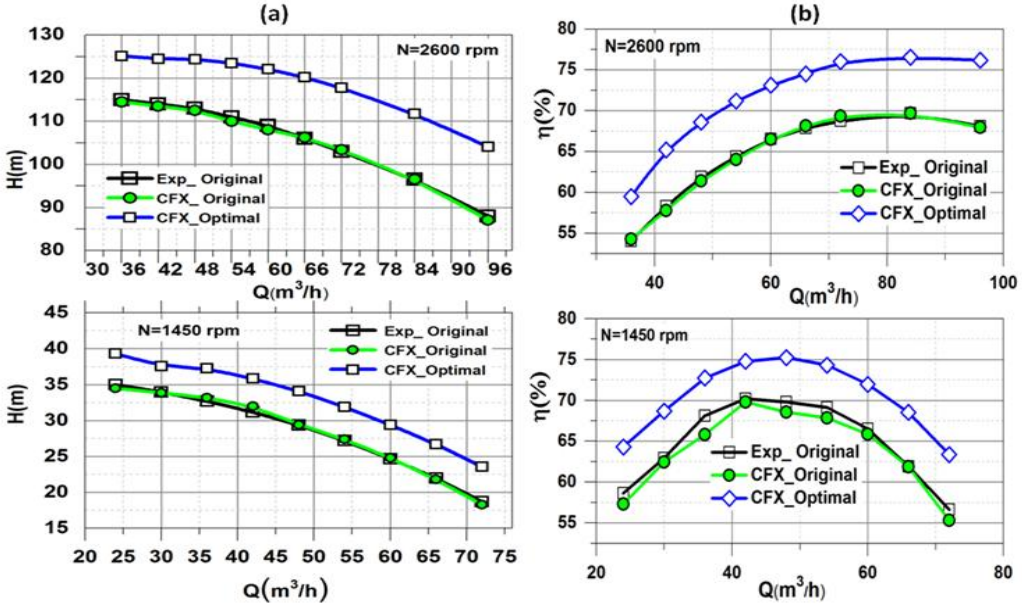

Fig. 11. Experiment and predicted performances comparison of the original and optimal multistage pump versus the flow rate and rotating speed: (a) head and (b) overall efficiency.

lower flow rates. Despite a 29% reduction in the optimum diffuser's throat area, BEP was not changed, indicating an oversized diffuser throat. The volute's throat area was crucial to BEP as it is located at the last stage; the latter was reduced by 1.2% while BEP was conserved. At N=2600 rpm, the gain in the head varied from 9.29% to 19.35%, although the overall efficiency reached 12.05%, up from 9.01%. However, at N=1450 rpm, the overall efficiency of the pump and head increased from 6.52% to 11.80%, and from 10.5% to 26%, respectively. The hydraulic efficiency curves for both stages are shown in Figs. 12(a) and 12(b); the curves demonstrated an improvement in efficiency at different flow rates, especially at the volute stage where maximum efficiency was obtained at high flow rate. According to Gülich (2010). The measurements exhibited a uniform velocity distribution at the impeller outlet where Q was between 80% and 90% of Q_{opt}; (η_h) shifted from BEP towards the low flow rates (Fig. 12(a)), as the overall efficiency was strongly dependent on the minimum hydraulic losses in all pump components, including flow leakages. The diffuser stage efficiency (Fig. 12(a)) was less than that of the volute at different optimal flow rates; this was probably due to the additional inter-stage leakage which could cause supplementary losses in the first impeller, with more losses observed in the diffuser and return channel. The hydraulic losses were mainly caused by frictions resulting from the shear stresses in the boundary layers on the walls, are strongly dependent on the Reynolds number. A decelerated and separated flow can lead to the

formation of thick boundary layers and stalled zones which could subsequently create jet-wake flow at the exit of the impeller can strengthen incidence losses at the leading edge of the collectors. Leakages can lead to the creation of pre-swirls which can prompt incidence losses at the impeller inlet. The volute's inlet was less sensitive than that of the diffuser for a non-uniform flow; however, the volute was fully affected by secondary flows, where the streamlines are presented by a double vortex in the cross sectional plane.

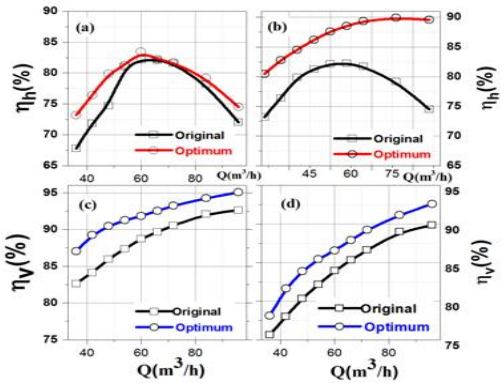

Fig. 12. Hydraulic and volumetric efficiencies of the stages versus the flow rate at N=2600 rpm: (a) and (c) first stage; (b) and (d) second stage.

Figures 12(c) and 12(d) show improvements in the volumetric efficiency of the optimized pump. The leakage flow rate was controlled by the pressure generated at the impeller outlet with the swirl factor being at the entrance of shroud as well as the hub gaps (Fig. 13). The flow leakage entered the gap with a very high tangential velocity, as it is the case with the optimized pump which tend to accelerate the fluid rotation in the gap between the impeller sidewalls and the stationary casing. Consequently, this resulted in an increase in the difference between the static pressures at the outlet of the impeller and at the seal entrance; it also created a pressure drop through the seal which could prompt a reduction in flow leakage. This behavior was previously confirmed by van Esch (1997).

6.3 Original and Optimal Pressure Recovery Contours in Collectors

The strong interactions between the impellers and collectors are shown in Fig. 14; these are located in the closed zone near the diffuser's leading edge and the volute's cutwater. The interactions are dominated by pressure losses. Enlarging the passage may favor pressure recovery which can be very important in the diffusing channel, downstream and upstream throats. The optimum diffuser was 20.26% longer than that of the original one, allowing better recovery in the upstream throat (Figs. 14(d), 14(c)). From Fig. 15, the optimal volute cross-sectional area decreased in the Θ range [67°-260°] and in the diffusion channel, also increased in the whole passage. When Θ was greater than 260°, the pressure recovery in the optimal volute (Fig. 14(b)) became more important than that of the reference volute (Fig. 14(a)); this was owing to an the increase in the passage area (Fig. 15) as well as the conversion of significant amounts of kinetic energy at the impeller's exit (Fig. 13). Similar observations were confirmed by

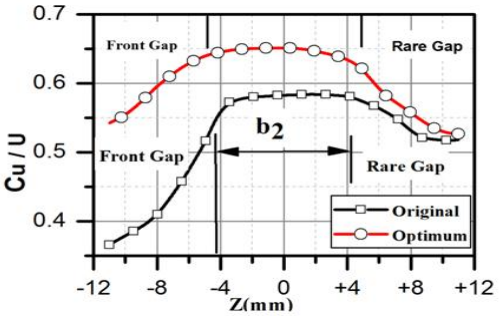

Fig. 13. Swirl factor at the outlet impeller and sidewalls gaps of the second stage at N=2600 rpm, Q=84 m³/h and t = 0.069228 s.

Wesche (2012). At the upstream throat (Fig. 14(b)), the residual energy was converted to pressure with minimum losses in the diffusing channel; the pressure loss was similar to that of a separate flow and secondary flow losses in a bended tube. By reducing the passage area (Fig. 15) and curvature angle, together with increasing the curvature radius, could minimize pressure loss.

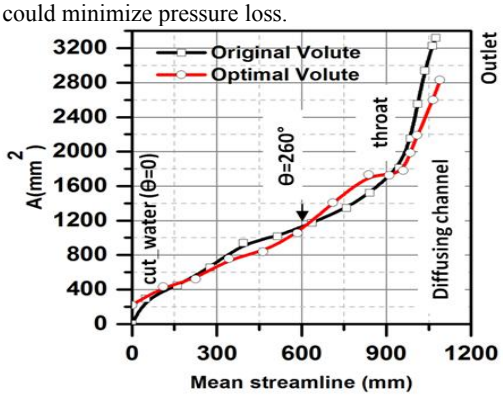

Fig. 15. Distribution of cross section area in the volutes.

6.4 Head and Pressure Fluctuation Comparison

The head fluctuations are shown in Fig. 16. The curves have seven periodicities over one revolution, corresponding to the number of impeller blade passing near the volute's cutwater. The new pump achieved 22.5% in amplitude reduction, with lower alternating stress mainly caused by a 4.86% increase in the distance between the impeller and the volute cutwater. According to Gülich *et al.* (1992), this space is one of the most important design parameters used to limit the amplitude of pressure pulsations generated at high circumferential speeds, as well as avoid causing fatigue to both the impellers and collectors. The fluctuation in pressure with respect to different angular positions of the impeller is shown in (Fig. 17). When θ=0, the volute's tongue become aligned with the blade's trailing edge. The pressure contours are slightly deformed in the optimized volute compared to those of the original one, this

behavior is explained by the less distorted velocity distribution in the wake, which is mainly caused by the presence of a tapered trailing edge and the large space between the cutwater and trailing edge.

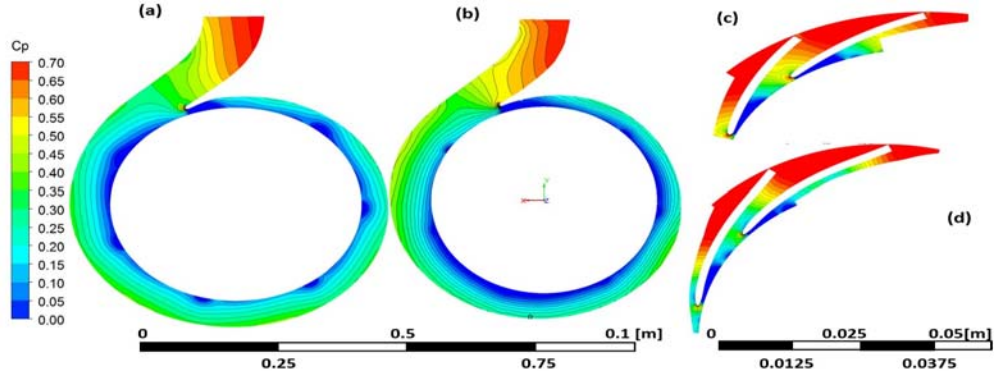

Fig. 14. Mid span static pressure recovery coefficient contours at Q=84 m^3/h and, N=2600 rpm and t= 0.069228 s: (a) original volute, (b) optimal volute, (c) original diffuser and (d) optimum diffuser.

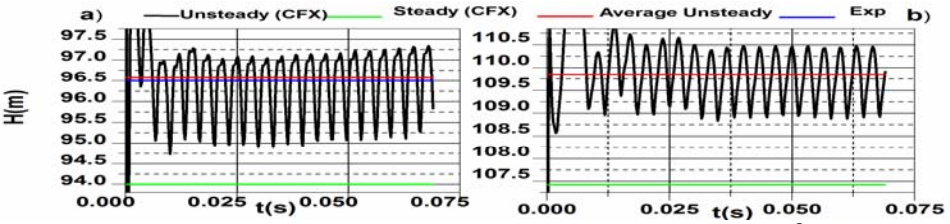

Fig. 16. Unsteady head comparison at N= 2600 rpm and Q=84 m^3/h.

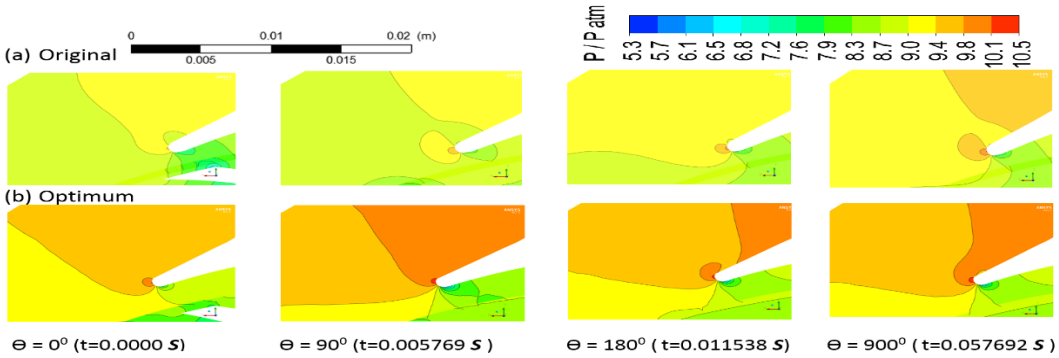

Fig. 17. Unsteady static pressure near the cut water of the volute at N= 2600 rpm and Q = 84 m^3/h: (a) original pump and (b) optimized pump.

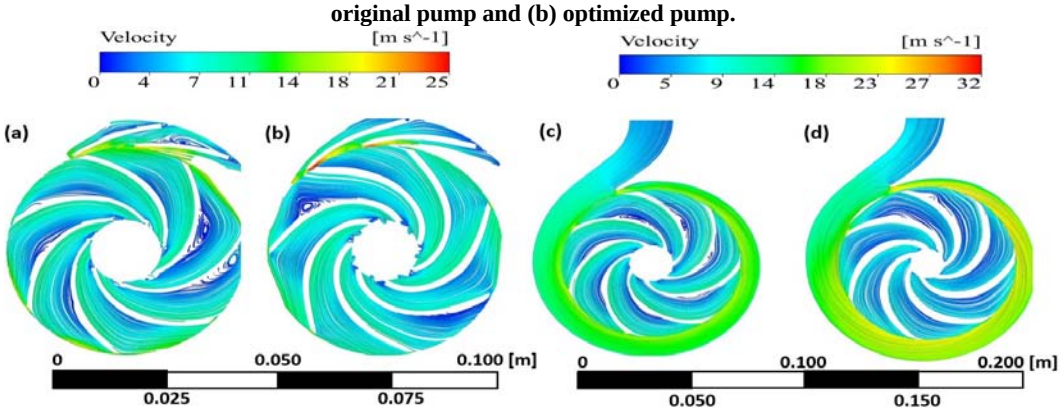

Fig. 18. Mid span streamlines colored by the relative flow velocity at N=2600 rpm , Q=48 m^3/h and t= 0.069228 s: (a) original first stage, (b) optimum first stage, (c) original second stage and (d) optimum second stage.

6.5 Streamline Comparison in Unsteady Flow Regime

The flow field structure in the impellers, created at low flow rate (Q=0.57Q_{opt}), is shown in Fig. 18; clear separations are observed on the pressure sides of the blades of the original pump owing to the presence of curvature shapes (Figs. 18(a) and

18(c)). On the other hand, the separation within the optimal impeller was only observed near the cutwater (Fig. 18(d)). Streamlines were identified by the accelerated flow in the spiral part, going through the narrow passage at elevated circumferential velocity, towards the impeller exit. The impeller-diffuser interaction of the optimum stage is shown in Fig. 18(b), In general, the flow was well guided, as previously seen, by the recirculation located near the impeller exit; contrary to the reference stage, the flow was fully separated including that of the diffuser (Fig. 18(a)).

7. CONCLUSIONS

The multi-objective optimization using NSGA-II algorithm coupled with CFD code allowed the combination of different solutions derived from both Pareto fronts, according to the required objectives and constraints. The optimized two-stage centrifugal pump provided much more changes in the meridional shapes. Improvements were visible throughout the operating range. A minimum improvement of 9.29% in head and 9.01% in overall efficiency was achieved at N=2600 rpm; in addition, up to 10.5% improvement in head and 6.52% in overall efficiency were obtained at N=1450 rpm. The hydrodynamic performance exhibited a better behavior in terms of flow stability, pressure loading and recovery. The predicted performances obtained from the unsteady state CFD analysis by considering leakage flows were in agreement with the experimental ones. The unsteady effects were attenuated owing to low fluctuations in the pressure amplitude, something which is required for safely operating the pump.

ACKNOWLEDGMENTS

The authors are grateful to the Professor A. Hamdi, and we are indebted to the pump designer Mr. Ahmed to carry out this research work.

REFERENCES

ANSYS Workbench Platform URL: http://www.ansys.com/Products/Platform.

Bratley, P. and B. L. Fox (1988). Algorithm 659: Implementing Sobol quasi-random sequence generator. *ACM Trans. Math. Software*, 14, 88-100.

Cvetković, D., H. Mühlenbein (1994). The optimal population size for uniform crossover and truncation selection. *Technical report* 94-11, GMD.

Dailey, J. W. and R. E. Nece (1960). Chamber dimension effects on frictional resistance of enclosed rotating disks. *ASME J. Basic Eng*, 82, 217-232.

Deb, K., A. Pratap, S. Agarwal and T. Meyarivan (2002 Apr). A fast and elitist multi-objective genetic algorithm NSGA-II. *IEEE Trans. Evol. Comp*, 6(2), 182-197.

Fang, H., Q. Wang, Y. T. U. and M. F. Horstemeye (2008). An efficient non-dominated sorting method for evolutionary algorithms. *IEEE Trans. on Evolutionary Computation*, 3(16), 355-384.

Feng, J. J., F. K. Benra and H. J. Dohmen (2009). Comparison of Periodic Flow Fields in a Radial Pump among CFD, PIV, and LDV Results. *International J. of Rotating Machinery*, Article ID 410838.

Gülich, J. (2010). *Centrifugal pumps*. Springer, Heidelberg Dordrecht London New York.

Gülich, J. F., U. Bolleter (1992). Pressure pulsations in centrifugal pumps. *ASME J Vibr Acoustics,* 114, 272 - 279.

Hirsch, C. and A. Ligout (2006 March). Multidisciplinary optimization of turbomachinery component. *VKI lecture series, introduction to optimization and multidisciplinary design*, 6-10, Brussels, Belgium.

Huang, R. F., X. W. Luo and B. Ji (2015). Multi-objective optimization of a mixed-flow pump impeller using modified NSGA-II algorithm. *Sci China Tech Sci*, 58(12), 2122 - 2130.

Jarmo, T. A. (1992). On optimal population size of genetic algorithms. In *Proceedings of the CompEuro92 Computer Systems and Software Engineering*, IEEE Comput Soc Pres, 65-70.

Knowles, J. and D. Corne (1999). The Pareto archived evolution strategy: A new baseline algorithm for multi-objective optimization. In *Proceedings of the 1999 Congress on Evolutionary Computation,* Piscataway, NJ, IEEE Press, 98-105.

Modefrontier 4.5 URL: http://www. esteco .com/modefrontier.

Nourbakhsh, A., H. Safikhani and S. Derakhshan (2011). The comparison of multi-objective particle swarm optimization and NSGA II algorithm: applications in centrifugal pumps. *Eng Optim*, 43(10), 1095-113.

Rovatti pompe. *Technical catalogue documentation:* Horizontal multistage high pressure pumps: SK80 performance, 17-20, URL: http://www.rovatti.it/pdf/SK80.pdf, July 25 01:02:44 2016.

Shi, L., R. J. Yang and P. Zhu (2012). A method for selecting surrogate models in crashworthiness optimization. *Struct Multidiscip Optimization*, 46(2), 159-170.

Srinivas, N., K. Deb (1995). Multi-objective function optimization using non-dominated sorting genetic algorithms. *Evol. Comput*. Fall, 2(3), 221–248.

Van esch, B. P. M. (1997). *Simulation of three-dimensional unsteady flow in hydraulic pumps*. Doctorate thesis, University of Twente, Netherlands.

Wesche, W. (2012). *Radiale Kreiselpumpen Berechnung und Konstruktion der hydrodynamischen Komponenten*. Springer, Heidelberg Dordrecht London New York.

Zhang, J. Y., H. W. Zhu and C. Yang *et al* (2011 January). Multi-objective shape optimization of helico-axial multiphase pump impeller based on NSGA-II and ANN. *Energy Conversion and Management*, 1(52), 538-546.

Zitzler, E. and L. Thiele (1998). Multi-objective optimization using evolutionary algorithms - A comparative case study. In *Parallel Problem Solving From Nature. V. A. E. Eiben, T. Bäck, M. Schoenauer, and H-P. Schwefel, Eds*. Berlin, Germany, Springer, Verla, 292-301.